

# Design, structural modeling, control, and performance of 20 MW spar floating wind turbines

Carlos Eduardo Silva de Souza <sup>\*</sup>, Erin E. Bachynski-Polić

*Department of Marine Technology, Norwegian University of Science and Technology, Trondheim, Norway*

## ARTICLE INFO

### Keywords:

Floating wind turbines  
Fatigue analysis  
Extreme analysis  
Hydroelastic modeling  
Wind turbine control systems

## ABSTRACT

As floating wind turbines (FWTs) increase in size and power, the relative contribution of wave and wind loads to their global responses differs from what has been observed for 5–10 MW units. In addition, the larger deflections at the platform, increased natural period range for some degrees of freedom, and larger RNA weight at higher heights invite a review on structural modeling methods, design constraints, dynamic analysis, and control systems. This paper explores these topics through the design and structural analysis of three spar-type 20 MW FWTs, with different constraints on the static pitch angle at rated wind speed. Time-domain simulations are performed with a non-linear aero-hydro-servo-elastic software, and sectional fatigue damage and extreme motions and axial stresses for the three designs are compared. The platform is modeled as a flexible body, with hydrodynamic loads evaluated with potential theory and distributed over the hull. A control system with a motion compensation strategy is adopted, ensuring the same controller bandwidth for the three FWTs and showing significant performance improvements compared to detuning the controller gains. In addition to impacting steel and ballast mass, the static pitch angle at rated thrust affects the platform dynamics and fatigue damage/extreme loads significantly. The platforms with larger restoring in pitch present less fatigue damage at the platform, but more at the tower. Extreme stresses are largely affected by gravitational loads, such that the designs with larger pitch at rated thrust have the highest extreme stresses at the platform and most of the tower sections. Load cases associated with the rated wind speed often govern the extreme loads, unlike previous studies with 5 MW and 10 MW FWTs.

## 1. Introduction

Floating wind technology has been progressing towards increased power per unit. Current projects planned to be built in the next 5 years comprise wind parks with 8–13 MW floating wind turbines (FWTs) [1–3], while wind turbines with nominal power of 14 MW [4] and 16 MW [5] are reaching commercial maturity — and academic research has investigated the feasibility of 20 MW [6–8], 25 MW [9], and even 50 MW [10] machines.

The increased wind loads and heavier turbines challenge the design and performance of their supporting structures. The dynamic behavior and structural integrity of FWTs have been extensively investigated in the last decade, benefiting in a broad extent from the NREL 5 MW [11] and DTU 10 MW [12] reference wind turbines. Larger FWTs will, however, have different natural periods and response to wind and wave loads — the structural dynamics of large wind turbines were listed by Veers et al. as one of the “grand challenges in wind energy science” [13]. Thus, the conclusions obtained from 5–10 MW structures may not necessarily apply to

<sup>\*</sup> Corresponding author.

E-mail address: [carlos.souza@ntnu.no](mailto:carlos.souza@ntnu.no) (C.E.S.d. Souza).

<https://doi.org/10.1016/j.marstruc.2022.103182>

Received 19 October 2021; Received in revised form 7 January 2022; Accepted 21 January 2022

Available online 4 March 2022

0951-8339/© 2022 The Author(s). Published by Elsevier Ltd. This is an open access article under the CC BY license

(<http://creativecommons.org/licenses/by/4.0/>).

those beyond 15 MW. In addition, appropriate methods to model and analyze the structural loads and coupled dynamics of large FWTs must be developed.

One point that needs further investigation relates to the modeling of FWTs as fully-flexible structures. While a significant volume of work models the platform as a rigid body, this assumption can be questionable when the dimensions increase and structural deflections become more important. Modeling the platform as a flexible body, on the other hand, requires the appropriate distribution of hydrodynamic loads over the structure [14–18]. The accuracy of the predicted sectional stresses on the platform can be compromised if radiation and diffraction loads are simplified, while computational time can increase significantly depending on how these loads are evaluated in time domain.

Cyclic loads in floating wind turbines are mainly caused by the action of wind, waves, and the loads associated with rotation of the blades and drivetrain machinery [19]. Kvittem and Moan [20] assessed fatigue damage calculation for a 5 MW semi-submersible FWT, considering bin size, simulation length, and number of realizations. Engebretsen et al. [18] compared fatigue damage for a 8 MW spar FWT when modeling hydrodynamic loads using Morison formulation and distributed potential theory (DPT), noting significant over-prediction when the former approach is adopted. Hegseth and Bachynski [21] assessed the distribution of fatigue damage over a 10 MW spar FWT platform and tower, in the context of design optimization.

Extreme axial stresses are important in the assessment of structural yielding and buckling. In addition, extreme platform pitch motions and nacelle fore-aft acceleration can cause large loads on the drivetrain and interruptions in production. For FWTs, extreme events result from the combination of harsh wave loads with the low-frequency motions induced by the wind. Karimirad and Moan [22] analyzed the extreme loads on a 5 MW spar FWT, finding extreme bending moments at the platform and tower to be associated with storm load cases – i.e., those corresponding to extreme wind conditions, when the turbine is idling. Li et al. [23] proposed to also consider the cut-off condition in the analysis for a 5 MW semi-submersible FWT, ensuring that load cases with an operating turbine are included — the rated condition, however, was found to be non-important for extreme loads for the platform considered.

Control systems play a significant role in the dynamic response of FWTs. Interaction with the FWT motions can provoke serious instabilities, resulting in large pitch motions and structural bending moments [24,25]. Controller “detuning” [26] is a common strategy to cope with this problem in academic research, but the method reduces the controller performance and can be unrealistic for larger FWTs, due to the increased pitch natural periods. Skaare et al. [27] used an observer to remove the influence of the FWT motions from the controller, avoiding the instability without needing to reduce the controller gains. A similar, but simpler method was proposed by Lackner [28], who used the FWT pitch velocity to modify the reference rotor speed. Hegseth et al. [29] used the latter method in the design optimization of 10 MW spar FWTs, obtaining reduced wall thickness for the tower compared with a design based on a detuned controller.

The objectives of this paper are to investigate the design, control system, and structural modeling considerations of 20 MW spar FWTs; and to perform a comprehensive dynamic and structural analysis, focusing on the relative importance of wind and wave loads on the fatigue life and extreme stresses at different locations of the platform and tower. Three spar FWTs supporting the 20 MW wind turbine from Ashuri et al. [6] are obtained from a parametric design process, with the diameters at the bottom and at sea water level (SWL) as design variables; the static pitch angle at rated wind speed constrained at 6°, 8°, and 10°; and the draft fixed at 90.0 m for all concepts. The entire structure is assumed as elastic, and modeled with finite elements. Hydrodynamic loads are evaluated with potential theory and distributed over the hull. A controller with motion compensation based on feedforward of the nacelle velocity is adopted, avoiding the instabilities related to controller-motion interactions. The analyses are based on fully-coupled, non-linear time-domain simulations, using an aero-hydro-servo-elastic software.

The parametric design of the platform, as well as adaptations to the original tower from Ashuri et al. [6] are presented in Section 2; the control system is introduced in Section 3, and the structural and hydrodynamic model is explained in Section 4; the dynamic analysis is described in Section 5, and results are presented and discussed in Section 6; conclusions are drawn in Section 7.

## 2. FWT design

### 2.1. 20 MW wind turbine model

Ashuri et al. [6] presented a 20 MW upwind, land-based wind turbine model, resulting from a multidisciplinary design optimization with constraints on structural life, modal frequencies, tip-speed ratio, and blade-tower clearance. The turbine is adopted in the present work, with some modifications related to its use on a floating platform.

One of the modifications is the tower design. The natural frequencies of the first tower bending modes of a bottom-fixed wind turbine are expected to increase when the same structure is installed on a floating platform [30]. Consequently, the shifted 1st fore-aft and side-side tower bending frequencies can lie within the 3p blade-passing range, rather than the soft-stiff range (Fig. 1), leading to resonant excitation and increased fatigue damage.

The tower is first shortened by 10 m, which is the desired height for the base above still water level (SWL). Then, the tower diameter and thickness are increased until the 1st bending frequency exceeds  $3 \times \Omega_r = 0.36$  Hz when the tower is installed on a floating platform, where  $\Omega_r$  is the rated rotor speed. By increasing the diameter of all the sections by a factor of 1.2, and keeping the diameter-to-thickness ratio of 160 [6], it is possible to obtain a 1st bending frequency ranging between 0.41–0.42 Hz (stiff-stiff), depending on the spar design. This solution is in line with the design optimization by Hegseth et al. [21], who found feasible solutions for stiff-stiff tower only, for a 10 MW FWT.

Although 6p excitation is not as critical as 3p, it is also desirable to avoid interactions at the 6p range. This is done by increasing the cut-in rotor speed to 4.2 rpm. This strategy avoids overlapping between the 3p and 6p ranges, allowing for the tower 1st bending frequency to be out of any blade-passing ranges. Table 1 shows the main properties of the wind turbine and tower, after the modifications. The mass and vertical centers of gravity (VCGs) (given with respect to SWL) are presented in Table 2.

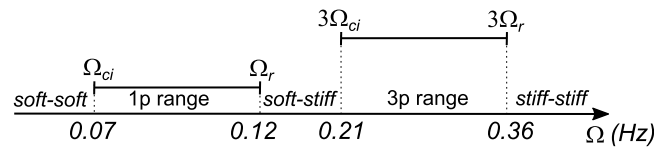


Fig. 1. Blade-passing frequency ranges for the 20 MW turbine.

**Table 1**  
20 MW wind turbine properties [6].

Number of blades	3
Rotor diameter (m)	276.0
Hub height (m)	160.2
Cut-in, rated, cut-off wind speed (m/s)	3.0, 10.7, 25.0
Cut-in <sup>a</sup> , rated rotor speed (rpm)	4.20, 7.15
Gear ratio	164.0
Generator efficiency (%)	94.4
Rated power (MW)	20.0
Tower base, top diameter <sup>a</sup> (m)	12.00, 7.44
Tower base, top thickness <sup>a</sup> (cm)	7.50, 5.58

<sup>a</sup>Indicates a modification from the original design.

**Table 2**  
Mass and VCG (w.r.t. SWL) of wind turbine components and tower.

Component	Mass (kg)	VCG (m)
Tower	$2.07 \times 10^6$	70.79
Blade $\times$ 3	$7.77 \times 10^5$	160.59
Hub	$2.53 \times 10^5$	160.20
Nacelle	$9.45 \times 10^5$	157.18

## 2.2. Spar parametric design

The spar is assumed to be a cylindrical, hollow structure, with constant thickness along its length and at the bottom plate. The diameter, however, is variable, so the platform is divided in three parts: the bottom, the mid, and the top (Fig. 2). The smaller diameter at the top is intended to reduce wave loading near the surface, at the price of lower hydrostatic restoring in heave. The mid part is tapered, with the diameter varying from the larger radius at the bottom to the shorter one at the top. The tower begins 10.0 m above SWL.

The fundamental constraint for the spar design is the weight–buoyancy balance, expressed by

$$(m_{hull} + m_{bal} + m_{tow} + m_{rna} + m_{moor})g = \rho g V_{sub}, \quad (1)$$

where  $m_{hull}$  is the hull steel mass;  $m_{bal}$  is the ballast mass;  $m_{tow}$  is the tower mass;  $m_{rna}$  is the rotor-nacelle assemble mass;  $m_{moor}$  is the mass-in-water of the mooring lines' hanging portion; and  $V_{sub}$  is the submerged volume of the platform. In addition, the following constraints are imposed for determining the solution space:

1. The draft ( $d$ ) is always 90.0 m, to cope with limitations on typical shipyard capacity and transportation to the wind park.
2. The bounds on the diameter of the top section are 10.0 m to 16.0 m, allowing for a compromise between restoring in heave and wave loading.
3. The bounds on the diameter of the bottom section are 15.0 m to 26.0 m.
4. The tapered section starts 6.0 m below SWL. The length of the tapered section is determined from the fixed taper angle (30 deg) and the diameters.
5. The metacentric height must be larger than 1.0 m [31].
6. The heave natural period must be longer than 25 s. The pitch natural period must be always 5.0 s longer than the heave natural period, to avoid coupling effects (reducing the likelihood of Matthieu instability).

The hull steel mass is obtained from the volume of the spar wall and base, with steel density ( $\rho_{steel}$ ) assumed as 7850.0 kg/m<sup>3</sup>. The ballast consists of a cylindrical column of high-density concrete, extending from the base of the spar to a height  $h_{bal}$ . The ballast density  $\rho_{bal}$  is assumed as 4000.0 kg/m<sup>3</sup>, which corresponds to commercially available high-density concrete [32].

The mooring system consists of 3 catenary chain lines. Despite the small contribution of the mooring system to the total FWT mass, disregarding it in Eq. (1) could result in significant miscalculation of the FWT draft, due to the low hydrostatic restoring in heave. The procedure for obtaining the mooring line length for a given required stiffness in surge follows the equations for quasi-static catenary mooring systems [33]. The necessary mooring stiffness in surge is normally dependent on the allowable platform excursion, and on the desired surge natural period. Only the latter is used as a constraint in this work, being specified as 120 s.

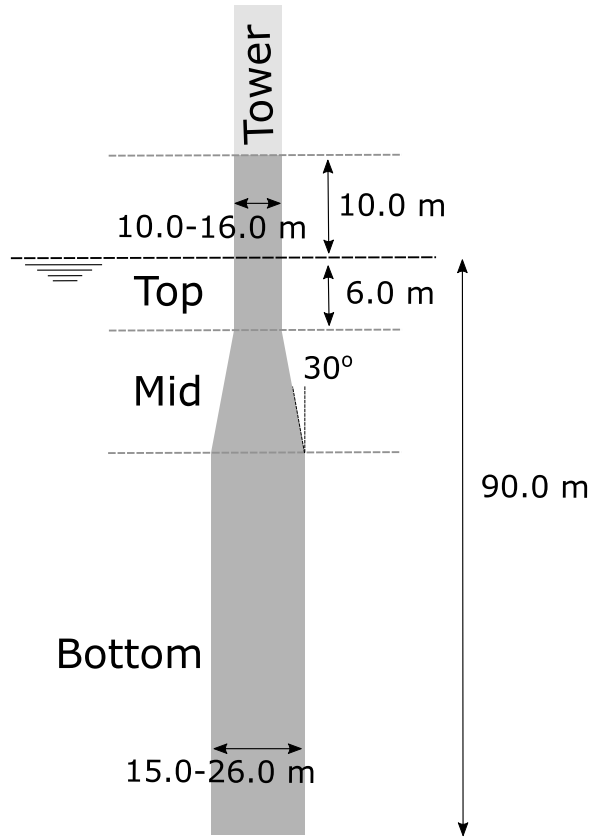


Fig. 2. Parts of the spar platform.

In order to estimate the natural periods during the parametric design stage, it is important to obtain a fair prediction of the added mass. The long-wave approximation for a cylinder is used to obtain the added mass coefficient in surge [34]:

$$a_{11} = \int_{-d}^0 a_1 dz = \rho\pi \int_{-d}^0 r(z)^2 dz, \tag{2}$$

where the section radius  $r$  varies along the platform. The added mass coefficients in pitch ( $a_{55}$ ) and coupled surge-pitch ( $a_{15}$ ) are obtained as follows:

$$a_{55} = \int_{-d}^0 a_1(r)z^2 dz = \rho\pi \int_{-d}^0 r(z)^2 z^2 dz, \tag{3}$$

$$a_{15} = \int_{-d}^0 a_1(r)z dz = \rho\pi \int_{-d}^0 r(z)^2 z dz. \tag{4}$$

For heave, the added mass is assumed as half of the displaced mass of the volume of a sphere with the same radius as the bottom section.

The linear restoring terms in heave and pitch are directly obtained from the dimensions and metacentric height of each candidate solution, respectively. For heave, the natural period is estimated based on an 1-DOF system. For pitch, coupling with surge is taken into account in a 2-DOF system. The latter system is also used for determining the static platform pitch angle at rated thrust,  $\theta_r$ . A MATLAB script is used for combining the platform dimensions and computing the corresponding inertia, volume, added mass, restoring coefficients, mooring properties, and natural periods — subjected to the constraints listed above.

### 3. Wind turbine control system

The control system consists of a variable speed, variable pitch (VSVP) approach, with a motion compensation strategy based on feedforward of the filtered nacelle velocity above rated wind speed. In addition, a peak shaving approach is adopted to limit thrust around rated wind speed. A modified version of the NREL ROSCO controller [35] is adopted, where the nacelle velocity feedforward approach is implemented.

**Table 3**  
Wind turbine control parameters.

Controller natural frequency (rad/s)	0.31
Controller rel. damping (-)	0.7
Nac. velocity feedforward gain (rad/m)	-6.4
Nacvel LP-filter cut-off frequency (rad/s)	0.18
Torque regime above rated	Constant power
Gen. torque const. in Region 2, HSS (N m s <sup>2</sup> /rad <sup>2</sup> )	11.99

### 3.1. Below rated

Following Ashuri et al. [6], the control strategy below rated rotor speed is based on the NREL 5 MW baseline controller, which combines an operational region for power optimization, with transitional regions near cut-in and rated rotor speeds. The corresponding parameters were obtained from the accompanying FAST model.

### 3.2. Above rated

Above rated wind speed, the original wind turbine model [6] adopted a proportional–integral (PI) controller to regulate the rotor speed error through the blade-pitch angle:

$$\Delta\beta = K_p\Delta\Omega + K_i \int_0^t \Delta\Omega dt, \quad (5)$$

with  $K_p$  and  $K_i$  being the proportional and integral gains. The rotor speed error  $\Delta\Omega$  is given by

$$\Delta\Omega = \Omega - \Omega_r, \quad (6)$$

where the reference  $\Omega_r = \Omega_0$  is the rated rotor speed.

Although this formulation provides satisfactory performance for a bottom-fixed turbine, its use in floating wind turbines can introduce resonant motions associated with controller-motion interaction [24–26]. Controller *detuning* is a common approach to deal with the problem. The idea is to reduce the gains, preventing the controller to respond to rotor speed variations caused by pitch motions.

Despite being widely used in academic research for FWTs, detuning reduces the controller's ability to cope with wind fluctuations on the order of the pitch natural period, leading to significant power fluctuations. In addition, excessive pitch motions can take place, leading to large structural loads and turbine shutdown [36]. Controller detuning is particularly problematic for the present work, since the pitch natural periods are relatively long compared with smaller FWTs. In addition, one of the main interests is to compare FWTs with different restoring – and thus natural periods – in pitch. A fair comparison between the different designs would then not be possible, since the controller bandwidths would vary for each FWT, affecting their dynamics significantly.

Lackner [28] avoided the instability associated with pitch motions by modifying the reference rotor speed as a function of the platform pitch velocity. In this work, an equivalent strategy is adopted, where the low-pass filtered nacelle velocity,  $v_{n,f}$ , is used to update  $\Omega_r$ :

$$\Omega_r(t) = \Omega_0 + K_{ff}v_{n,f}, \quad K_{ff} < 0. \quad (7)$$

Including the time-varying  $\Omega_r(t)$  in the rotor speed error (Eq. (6)) is equivalent to informing the controller whether the turbine is moving downwind or upwind, preventing it from responding to rotor speed fluctuations caused by the platform motions. This approach is thus known as feedforwarding of the nacelle velocity.

The platform pitch response to waves, although relatively low, can be amplified by the long arm from the center of rotation to the nacelle. Therefore, the nacelle velocity is low-pass filtered to avoid wave-frequency components being fed into the controller through  $\Omega_r(t)$ . A 2nd-order Butterworth filter was found to provide satisfactory filtering performance. Stability of the controller is verified based on a linearized system [37], including states from the nacelle motion, the rotor speed, and 2nd-order low pass filter. First-order aerodynamic derivatives were obtained using FAST's linearization module.

The PI controller with feedforward of the nacelle velocity allows the same controller natural frequency  $\Omega_{ctrl}$  to be used for all spar designs.  $\Omega_{ctrl}$  corresponding to 20 s, just longer than the typical wave frequency range, avoids interactions with wave responses. A gain-scheduling strategy is implemented in the form of a look-up table, to ensure that the required natural frequency is maintained for all blade pitch angles. The main parameters of the above-rated controller are provided in Table 3.

### 3.3. Peak shaving

Peak shaving is a strategy based on starting to pitch the blades just before rated wind speed, thus limiting the thrust and reducing structural loads [38]. The implementation in ROSCO consists of a look-up table where the minimum blade pitch angle is set as a function of the low-pass filtered wind speed. Instead of peaking at rated, the thrust then becomes flat at the range where peak shaving is active.

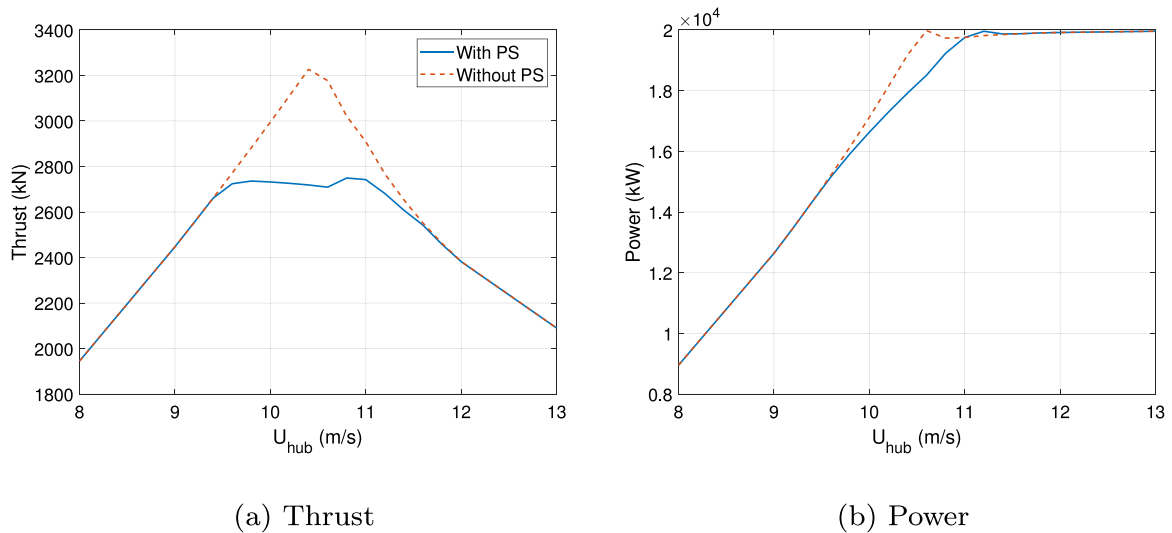


Fig. 3. Thrust and power curves with and without peak shaving.

A consequence of peak shaving is a reduction of power capture just below the rated wind speed, which depends on the level of reduction in thrust required. In this work, the thrust is limited to  $2.8 \times 10^6$  N, corresponding to ca. 87% of the original peak thrust at rated wind speed. Fig. 3 compares the thrust and power curves with and without peak shaving, for wind speeds close to rated. When peak shaving is active, a loss of power is observed for wind speeds between 9.5 m/s and 11.0 m/s, reaching up to 8% for  $U = 10.6$  m/s.

#### 4. Hydroelastic modeling

A consistent representation of the actual structural deflections, as well as of the hydrodynamic loads, is needed for accurately predicting the platform internal loads at the sections of interest. Two main approaches can be used for representing structural flexibility: a finite-element (FE) model, with the hydrodynamic loads distributed over the structure [14,16–18]; or a model based on modal superposition, with additional (generalized) degrees of freedom in order to represent flexible modes and the associated hydrodynamic loads [15,39,40].

The former approach is adopted in this work. The spar platforms are represented with FE beam elements, and divided in sections where the hydrodynamic loads are applied. Radiation and diffraction loads from 1st-order potential theory are applied at each section, combined with quadratic drag terms.

##### 4.1. Simulation tool

The simulations are carried out using SIMA, which performs coupled time-domain analyses combining the software RIFLEX and SIMO [41]. RIFLEX [42] is a finite element (FE) software for structural analysis of slender marine structures, and is used in this work for modeling the platform, tower, and wind turbine blades. It also computes the wind turbine aerodynamic loads using a blade element momentum (BEM) formulation, with Glauert's correction for high induction factors and Prandtl's correction factors for losses associated with the hub and blade tip. Øye's formulations for dynamic wake and dynamic stall are also included in the code. Hansen [43] provides details on the BEM method, as well as the corrections mentioned above. Tower shadow is accounted for based on 2-D potential flow around a circle.

SIMO [44] is a simulator of marine operations for large bodies. In this work, it is used for modeling global linear damping, 2nd-order wave forces, the mooring system, and the nacelle inertia properties. Skaare et al. [36] presented a comparison between simulations using SIMA with measurements from a real 2.3 MW spar floating wind turbine.

All realizations were run for a total of 4000 s, where the initial 400 s were assumed as transient and removed from the analyses. A time-step of 0.005 s was used for all cases. In order to improve numerical stability of the FE model, a global stiffness-proportional Rayleigh damping factor of  $2.5 \times 10^{-3}$  was adopted in all simulations, while mass-proportional damping was not used to avoid artificially damping LF modes [45]. The inclusion of numerical damping results in an increase of about 0.3% in the global relative damping at the 3p frequency (0.40 Hz), which is the highest relevant frequency of excitation in the system.

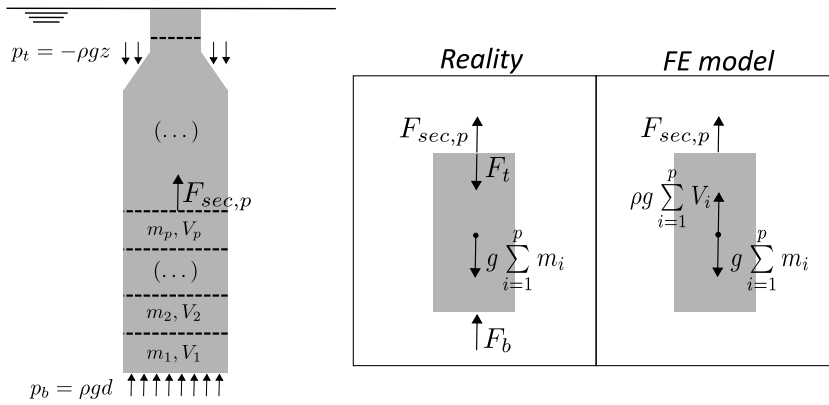


Fig. 4. Sectional axial force from hydrostatic equilibrium for an upright spar — the free-body diagrams illustrate the difference between the force obtained with the FE model and the analytical solution.

#### 4.2. Structural model

##### 4.2.1. Platform

The spar platform is modeled in RIFLEX using beam elements, with axisymmetric cross sections. The platform is subdivided in segments, on which the hydrodynamic loads are applied. The length of each segment varies according to its vertical position, but is limited to 5.0 m at the bottom and mid parts; and 3.0 m at the top part. Since the lower position of the mid part varies according to the design, the hull discretization varies slightly among the different spars.

The cross-sectional mass is determined based on the section diameter and thickness, and on the steel density given in Section 2. A steel modulus of elasticity  $E = 2.0 \times 10^{11}$  Pa is assumed for calculating the axial and bending stiffness. Since the torsional mode is not of interest for this work, an excessively large value was assigned to the torsional stiffness. For the portion filled with ballast, the mass is correspondingly increased, but the stiffness is assumed to remain unchanged.

In RIFLEX, the buoyancy and weight are applied at the center of each section. From the static equilibrium of forces in Fig. 4, the mean axial force at the  $p$ -th section is given by

$$F_{sec,i}^{FE} = W_p - B_p = g \sum_{i=1}^p (m_i - \rho V_i), \tag{8}$$

where  $m_i$  and  $V_i$  are the mass and volume of each section. For a real spar, however, the buoyancy in an undeflected position will be determined by the pressure distribution at the bottom and at the tapered segment. At the bottom, an upward force  $F_b$  is applied:

$$F_b = \rho g d \pi \frac{D_b^2}{4}, \tag{9}$$

where  $d$  is the draft and  $D_b$  is the base diameter. Thus, below the mid (tapered) section, the following correction must be considered for the axial force:

$$F_{sec,i}^{bot} = F_{sec,i}^{FE} + \rho g \left( \sum_{i=1}^p V_i - d \pi \frac{D_b^2}{4} \right). \tag{10}$$

At the mid (tapered) part, the pressure integration of the hull results in a downward force with magnitude:

$$F_t = -\rho g z \pi \frac{D_b^2 - D_s^2}{4}, \tag{11}$$

where  $z$  is the vertical position of the section and  $D_s$  is the section diameter. The correction at this part of the platform becomes:

$$F_{sec,i}^{mid} = F_{sec,i}^{FE} + \rho g \left[ \sum_{i=1}^p V_i - d \frac{\pi}{4} (d D_b^2 + z D_b^2 - z D_s^2) \right]. \tag{12}$$

For the top part, the upward force corresponds to the platform buoyancy. The correction is then given by:

$$F_{sec,i}^{corr} = F_{sec,i}^{FE} + \rho g \left( \sum_{i=1}^p V_i - V \right). \tag{13}$$

This correction is particularly important for the extreme analysis, especially for the sections closer to the spar bottom. For the fatigue analysis, on the other hand, it has a minor impact, since dynamic variations in the axial force have only minor contribution to the axial stresses, compared with the bending moments.

#### 4.2.2. Wind turbine

The wind turbine blades are modeled with 19 beam elements, using double-symmetric cross sections. The structural and geometrical properties, as well as the airfoil coefficients, are obtained from the FAST model which accompanies the wind turbine definition [6]. The hub and nacelle inertia properties are also obtained from the same model.

The tower is modeled with 20 beam elements, using thin-walled cross sections. The inertia and stiffness properties are obtained similarly as for the platform.

#### 4.3. Mooring system

The mooring system is modeled as a quasi-static system. An equivalent matrix of horizontal stiffness coefficients is found based on the mooring line mass and length, as well as fairlead and anchor positions, and based on catenary equations. Dynamic effects associated with velocity and acceleration of the line are not taken into account.

In order to increase the restoring arm in yaw, spar mooring systems typically include a “crow-foot” arrangement [36,46]. This configuration is not considered in the simplified mooring model adopted in this work. Instead, a linear stiffness coefficient in yaw is added at fairlead position to represent the crow-foot system, chosen to provide a natural period of 16.0 s in yaw for all designs. This is sufficiently longer than the cut-in 1p excitation period of 14.3 s, avoiding resonant yaw motions.

#### 4.4. Hydrodynamic model

The 1st-order potential theory loads are obtained with WAMIT [47], with the spars assumed as rigid bodies. The mesh is created ensuring that panels are not intersected by the sections defining the segments, so that each segment contains whole panels only. The panel length is kept at approximately 1.0 m through the entire mesh. Wave periods from 3.0 s to 25.0 s, with steps of 1.0 s, were adopted in the computation of hydrodynamic loads.

WAMIT offers the option to output the complex panel pressures corresponding to the radiation and diffraction problems, separately. It is then possible to reconstruct the radiation coefficients and excitation transfer functions in 3 (translational) DOFs for each spar segment, using the pressures at the corresponding panels and the fundamental equations of potential theory (see e.g. Svendsen [14]). RIFLEX then evaluates the diffraction and radiation loads in the time domain simulations. The latter requires the solution of convolution integrals of the retardation functions [48,49], which can be time-consuming when the number of sections is large. These integrals are approximated by the software as series of exponential functions, to reduce computational time. See e.g. Taghipour et al. [50] for details on this approach. Viscous drag is added based on a quadratic model, with the non-dimensional transverse drag coefficient  $C_d = 0.6$  for all the sections [51]. Drag loads in the longitudinal direction are not included.

The reconstruction of radiation coefficients from the distributed model does not result in a perfect representation for roll and pitch. For these DOFs, the method approximates the loads by the summation of lumped forces in surge and sway, respectively, multiplied by the squared distance from each segment to the origin – i.e., the fluid perturbation associated with the rotations are neglected. Fig. 5a compares the rigid-body and reconstructed pitch added mass for Spar8, whose dimensions are presented later in Table 8. The reconstructed coefficients are somewhat larger than their rigid-body counterparts. The difference is lower than 5% for the entire range of periods. Excitation loads are not affected by the same problem, but can be influenced by the hull discretization. Fig. 5b shows that the curves for excitation in pitch are nearly coincident, indicating that the hull discretization is satisfactory.

In addition to the distributed hydrodynamic loads over the body, the hydrodynamic model also includes a global linear damping matrix, in surge, sway, heave, and yaw. The damping coefficients are added to avoid unrealistic resonant responses at these DOFs. The criterion was to reach the same relative damping coefficients as obtained for the OC3Hywind spar [46].

##### 4.4.1. Difference-frequency 2nd -order wave loads

Due to the large size and low natural frequencies of rigid body motions of the platforms, it is of interest to include the difference-frequency second order wave loads. This effect can be accounted for with quadratic transfer functions (QTFs), obtained from the solution of the second-order potential in addition to second-order terms of the first-order potential.

The QTFs were calculated for the spars using WAMIT, considering difference frequencies up to 0.28 rad/s. This range covers the natural periods of all DOFs except yaw (which is not excited by waves for a spar). In WAMIT, it is possible to approximate the computation of the second-order potential by neglecting the integration of the quadratic forcing over the free surface, avoiding the discretization of this area and reducing computational time significantly. Simos et al. [52] evaluated this approximation for a 5 MW semi-submersible FWT, finding very good agreement with the QTF computed with the complete second-order solution. Free-surface effects are expected to be even less important for a spar, due to its simpler geometry and larger draft, and the procedure is thus adopted in this work also.<sup>1</sup>

The difference-frequency 2nd-order wave loads are not distributed over the hull. Instead, they are applied as a nodal load on the center of the spar, at mean water line.

<sup>1</sup> The adoption of Newman's approximation [53], on the other hand, is not recommended, due to the relatively short natural periods in heave, pitch, and roll.

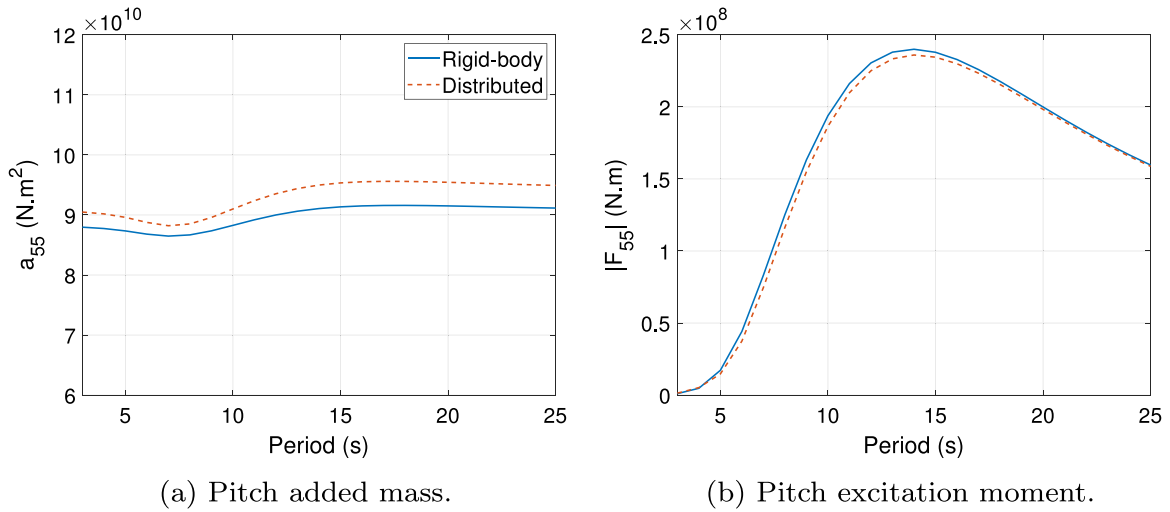


Fig. 5. Pitch added mass and pitch excitation moment amplitude for  $0^\circ$  incident waves. Comparison between rigid-body and reconstructed from distributed model.

## 5. Dynamic analysis

### 5.1. Environmental conditions

The fatigue and extreme analyses are performed considering the environmental conditions for the Norwegian Sea, Site 14 from Li et al. [54]. The long-term joint probability distributions of hub mean wind speed ( $U$ ), significant wave height ( $H_s$ ), and wave peak period ( $T_p$ ) are used for obtaining the most probable sea states associated with the wind turbine operational conditions, as well as the environmental contours corresponding to the 50-year cases. The distributions are obtained based on 10 years data from a numerical hindcast model. The water depth is set to 320.0 m.

The joint distribution of wind speed, wave significant height, and wave peak period, may be approximated by [54]

$$f_{U,H_s,T_p}(u, h, t) \approx f_U(u)f_{H_s|U}(h|u)f_{T_p|H_s}(t|h), \tag{14}$$

where  $f_U(u)$  is the marginal distribution of the mean wind speed;  $f_{H_s|U}(h|u)$  is the conditional distribution of significant wave height, for a given mean wind speed; and  $f_{T_p|H_s}(t|h)$  is the conditional distribution of wave peak period, for a given significant wave height.<sup>2</sup>

The marginal distribution of the one-hour mean wind speed at 10 m height,  $U_{10}$ , is assumed to follow a two-parameter Weibull distribution, with a probability density function (PDF) given as follows:

$$f_{U_{10}}(u) = \frac{\alpha_U}{\beta_U} \left(\frac{u}{\beta_U}\right)^{\alpha_U-1} \exp\left[-\left(\frac{u}{\beta_U}\right)^{\alpha_U}\right], \tag{15}$$

where  $\alpha_U$  and  $\beta_U$  are the shape and scale parameters, respectively, and are given in Table 4. Wind shear is assumed to follow a power law profile:

$$U(z) = U_{10} \left(\frac{z}{10}\right)^{\alpha_{PL}} \tag{16}$$

where the exponent  $\alpha_{PL}$  is assumed as 0.14 for all wind speeds.

The PDF for the conditional distribution of the significant wave height,  $H_s$ , for a given  $U$ , is also given by a two-parameter Weibull distribution:

$$f_{H_s|U}(h, u) = \frac{\alpha_{HU}}{\beta_{HU}} \left(\frac{h}{\beta_{HU}}\right)^{\alpha_{HU}-1} \exp\left[-\left(\frac{h}{\beta_{HU}}\right)^{\alpha_{HU}}\right], \tag{17}$$

with the parameters  $\alpha_{HU}$  and  $\beta_{HU}$  given by

$$\begin{aligned} \alpha_{HU} &= a_1 + a_2 u^{a_3} \\ \beta_{HU} &= b_1 + b_2 u^{b_3}. \end{aligned}$$

The coefficients  $a_i, b_i$  are provided in Table 4.

<sup>2</sup> Rigorously, the conditional distribution of wave peak period for a given pair of mean wind speed and significant wave height,  $f_{T_p|U,H_s}(t|h, u)$ , should be used in Eq. (14). The simplification is proposed by Li et al. [54] and is not expected to affect the estimate of critical conditions significantly.

**Table 4**  
Distribution parameters for site 14 of Li [54].

$\alpha_U$	2.029
$\beta_U$	9.409
$a_1$	2.136
$a_2$	0.184
$a_3$	1.000
$b_1$	0.534
$b_2$	0.070
$b_3$	1.435
$c_1$	1.886
$c_2$	0.365
$c_3$	0.312
$d_1$	0.001
$d_2$	0.105
$d_3$	-0.264

The conditional distribution of wave peak period on the significant wave height is assumed to follow a log-normal distribution:

$$f_{T_p|H_s}(t|h) = \frac{1}{\sqrt{2\pi}\sigma_{TH}t} \exp\left[-\frac{1}{2}\left(\frac{\ln t - \mu_{TH}}{\sigma_{TH}}\right)^2\right], \quad (18)$$

where the distribution mean  $\mu_{TH}$  and variance  $\sigma_{TH}$  are given by

$$\begin{aligned} \mu_{TH} &= c_1 + c_2 h^{c_3} \\ \sigma_{TH}^2 &= d_1 + d_2 \exp(d_3 h), \end{aligned}$$

with the coefficients  $c_i$  and  $d_i$  as provided in Table 4.

### 5.1.1. Environmental modeling

Waves are generated from time-domain realization of a three-parameter JONSWAP spectrum [33], with a  $\gamma$ -factor of 3.3 for all sea states. Long-crested waves are assumed.

Wind turbulence time series are generated using TurbSim [55], based on a Kaimal spectrum and with turbulence intensity following IEC Normal Turbulence Model category B [56] for all conditions. Wind shear is taken into account assuming a power law with exponent 0.14 for all wind speeds.

## 5.2. Fatigue analysis

A full long-term fatigue analysis includes all the possible combinations of mean wind speed, significant wave height, and wave peak period. As the present work focuses on the comparison between the different designs, the adopted fatigue analysis considers only the *most probable* sea state associated with each mean hub-height wind speed in the operational range.

Kvittem [20] showed that, for a 5 MW semi-submersible FWT, 4 realizations of 1h-simulations provide fatigue damage estimates within 5% of estimates based on 10 3-hour realizations. It is assumed that these conclusions are also valid for the FWTs of this work, such that the fatigue analyses are based on 4 realizations of 1h-simulations.

The most probable sea state associated with each mean hub wind speed corresponds to the  $H_s$  and  $T_p$  providing the highest value of the PDF's given by Eqs. (17) and (18), respectively. The mean hub wind speeds cover the turbine operational range from 4.0 m/s to 25.0 m/s with steps of 1.0 m/s. The probability of occurrence associated with bins centered at each mean wind speed, and bounded with  $\pm 0.5$  m/s, is obtained from Eq. (15).

### 5.2.1. Fatigue damage calculation

The fatigue analysis is based on DNV-RP-C203 [57], which recommends bi-linear S-N curves for offshore structures subjected to wind and wave loads. The accumulated damage is calculated at different sections of the platform and tower. All the conditions analyzed assume aligned wind and wave loads. The 1-hour fatigue damage accumulation  $D_{1h}$  is estimated from the average axial stress time-series of the 4 realizations, which are obtained from each section's axial force  $N_x$  and fore-aft bending moment  $M$  time-series according to:

$$\sigma_x = \frac{N_x}{A} + \frac{Mr}{I_y}, \quad (19)$$

where  $A$  is the annular section area,  $r$  is the section radius, and  $I_y$  is the section modulus around the bending axis.

A rainflow cycle counting procedure is then applied to the axial stress time series, providing a series of cycles with stress range  $S_i$ . The accumulated damage  $D_{1h}$  is obtained from:

$$D_{1h} = \frac{1}{a_1} \sum_{i=1}^{n_l} S_i^{m_1} + \frac{1}{a_2} \sum_{j=1}^{n_h} S_j^{m_2}, \quad (20)$$

**Table 5**  
Load cases considered in the fatigue analysis — operational conditions.

$V_{hub}$ (m/s)	$P(V_{hub} \pm 0.5)$ (%)	$I$ (%)	$H_s$ (m)	$T_p$ (s)
4.0	3.75	30.1	1.49	9.3
5.0	4.51	26.2	1.56	9.4
6.0	5.14	23.6	1.64	9.4
7.0	5.63	21.7	1.73	9.5
8.0	5.98	20.3	1.83	9.6
9.0	6.18	19.2	1.95	9.7
10.0	6.23	18.3	2.07	9.8
11.0	6.17	17.6	2.21	9.9
12.0	5.97	17.0	2.35	10.1
13.0	5.69	16.5	2.51	10.1
14.0	5.33	16.1	2.68	10.3
15.0	4.91	15.7	2.85	10.4
16.0	4.46	15.4	3.04	10.5
17.0	3.98	15.1	3.24	10.6
18.0	3.51	14.9	3.44	10.8
19.0	3.05	14.6	3.66	11.0
20.0	2.61	14.4	3.89	11.1
21.0	2.21	14.2	4.12	11.2
22.0	1.84	14.1	4.37	11.4
23.0	1.51	13.9	4.62	11.5
24.0	1.23	13.8	4.88	11.7
25.0	0.99	13.6	5.15	11.8

**Table 6**  
S-N curve coefficients and stress limit for spar and tower sections [57].

	Spar	Tower
$\bar{a}_1$	$1.0 \times 10^{11.764}$	$1.0 \times 10^{12.164}$
$\bar{a}_2$	$1.0 \times 10^{15.606}$	$1.0 \times 10^{15.606}$
$m_1$	3.0	3.0
$m_2$	5.0	5.0
$S_{lim}$ (MPa)	52.63	52.63

where  $n_l$  and  $n_h$  are the number of cycles in the low and high cycles regions, respectively. The stress limit  $S_{lim}$  dividing the regions, as well as the coefficients  $\bar{a}_{1,2}$  and  $m_{1,2}$  defining the S-N curves, are obtained from DNV [57] and are reproduced in Table 6. For the platform sections, the curves in seawater with cathodic protection are adopted, while for the tower the curves in air are used. A circumferential butt weld made from both sides is assumed for the spar and tower sections. The thickness effect is accounted for by modifying the stress ranges as recommended by DNV [57]. Stress concentration factors due to misalignment and thickness in butt welds are not considered in the analyses.

The damage associated with each of the load cases in Table 5 is then weighted with the probability of occurrence of the respective bin, providing the averaged 1-hour accumulated fatigue  $\bar{D}_{1h}$  at the platform and tower sections, for each spar.

### 5.3. Extreme analysis

A full long-term analysis (FLTA) is too time-consuming for practical prediction of extreme responses. In addition, usually a limited number of conditions govern the tail of the extremes distribution, such that methods for selection of these conditions are normally adopted in practice.

For floating wind turbines, Li et al. [23] proposed a *modified environmental contour method* (MECM), where the cut-off condition is also considered in addition to the 50-year environment. The idea is to account for cases where the turbine is not parked, as it is normally the case for the 50-year condition, such that loads related to thrust are also included in the analysis.

This approach is used for the analysis of extreme loads in this work, but the condition associated with the rated wind speed, which gives the largest mean thrust, is also added. Time-domain simulations are carried out for the 3 spars and considering each load case, with 20 realizations for waves and wind. For the case with 50-year hub wind speed, the turbine is set to idle with no generator torque and blades feathered to 88 degrees.

#### 5.3.1. Load case selection for the extreme analysis

In the MECM, as adopted here, the sea states forming 50-year contours with three mean hub wind speeds (rated, cut-off, and 50-year wind) are selected. In other words, the 3-D surface formed by combinations of  $U$ ,  $H_s$ , and  $T_p$  yielding a 50-year return period is “sliced” at the wind speeds of interest. The determination of the wind speed and sea state parameters is more easily done by transforming the random environmental variables (X-space) to a space where the variables follow a standard normal distribution (U-space):

$$F_{X_i}(x_i) = \Phi(u_i), \quad (21)$$

**Table 7**  
Hub mean wind speeds, turbulence intensity, and associated sea state parameters representing the environmental contours.

$U$ (m/s)	$I$ (%)	$H_s$ (m)	$T_p$ (s)	ID
10.7	17.8	2.39	3.57	i-rt
		3.62	4.64	ii-rt
		4.85	6.04	iii-rt
		6.08	7.99	iv-rt
		7.31	13.00	v-rt
25.0	13.6	3.92	5.11	i-co
		5.60	6.34	ii-co
		7.28	7.84	iii-co
		8.96	9.76	iv-co
		10.63	14.07	v-co
49.1	12.1	13.97	15.14	i-50

where  $i = 1, 2, 3$  and  $F$  and  $\Phi$  are the cumulative density functions in the respective spaces. The points in the U-space corresponding to a given return period form a sphere, which after transformation back to the X-space, provides the wind and sea state combinations with the required return period.

From the 50-year contour, the point providing the 50-year wind speed is associated with one combination of  $H_s$  and  $T_p$  only. For the rated and cut-off cases, there will be infinite combinations of  $H_s$  and  $T_p$  associated with the respective wind speeds, from which five are chosen for analysis according to the following wave height and steepness criteria:

- the combination with highest  $H_s$ ;
- the combination with largest  $H_s/T_p$  ratio;
- three conditions at the lower half of the contour, equally spaced between the two previous ones.

The resulting load case combinations are provided in Table 7, and illustrated in Fig. 6.

### 5.3.2. Extreme response calculation

For the extreme response estimate, a Gumbel distribution is fit to the maxima from the 20 realizations using the MATLAB toolbox WAFO [58]. The 90% fractile of the corresponding cumulative density function (CDF) is then used to obtain the 50-year axial stresses. In addition to the axial stresses, extreme values are also obtained for the platform extreme pitch angle and for the nacelle acceleration, following the same procedure.

## 6. Results

### 6.1. Spar dimensions

A total of 660 feasible solutions resulted from the parametric design process. Fig. 7 shows the steel and ballast mass as a function of the static pitch angle at rated, for all the solutions. As noted, the requirement of larger restoring in pitch demands up to 30% larger ballast mass. An increase in steel mass of up to 10% is also observed, due to the larger platform diameter.

The solutions are divided in groups with  $\theta_r \leq 6^\circ, 8^\circ$ , and  $10^\circ$ . The solution with lowest steel mass is chosen from each group. Table 8 shows the main dimensions for each of the spars. In addition to having reduced steel and ballast mass, the solutions with lower restoring in pitch also have lower diameter at the top, and thus reduced wave loading. The displayed natural periods are obtained from decay simulations, thus accounting for radiation effects from potential theory, and viscous damping. The natural period in pitch is significantly affected, with a difference of 10.4 s between Spar6 and Spar10. The difference in mooring system mass is due to the requirement of same natural period in surge — platforms with lower mass require lower restoring, and thus lighter mooring lines. It is noted that the actual surge periods are slightly different than 120.0 s, due to the adoption of simplified added mass and disregarding damping in the parametric design process. The different platform designs do not affect the tower bending frequencies significantly.

Since the different designs have different FE meshes, the platform sections considered in the analysis are placed at slightly different distances from the keel. The exact positions of the sections for each platform are given in Table 9. For all spars, Sections 1–6 are located at the bottom part of the platform; Section 7 is at the tapered part; and section 8 is at the waterline (top part). For the tower (Table 10), the section positions are the same for all designs.

### 6.2. Control system performance

In addition to responding more promptly to changes in the wind speed, the controller with motion compensation also provides more aerodynamic damping to the pitch motions, compared with the detuned controller. This becomes clear when analyzing the closed-loop system eigenvalues, as shown in Fig. 8 for Spar6, under a mean wind speed of 13.0 m/s. The detuned controller gains

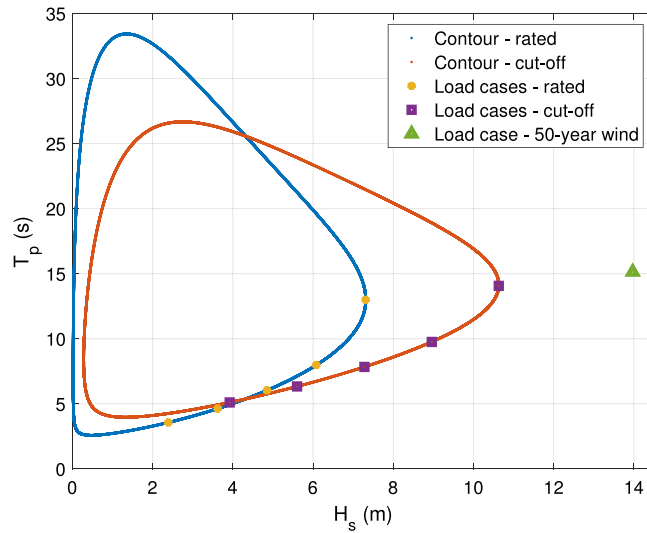


Fig. 6. Environmental contours and load cases for the extreme analysis.

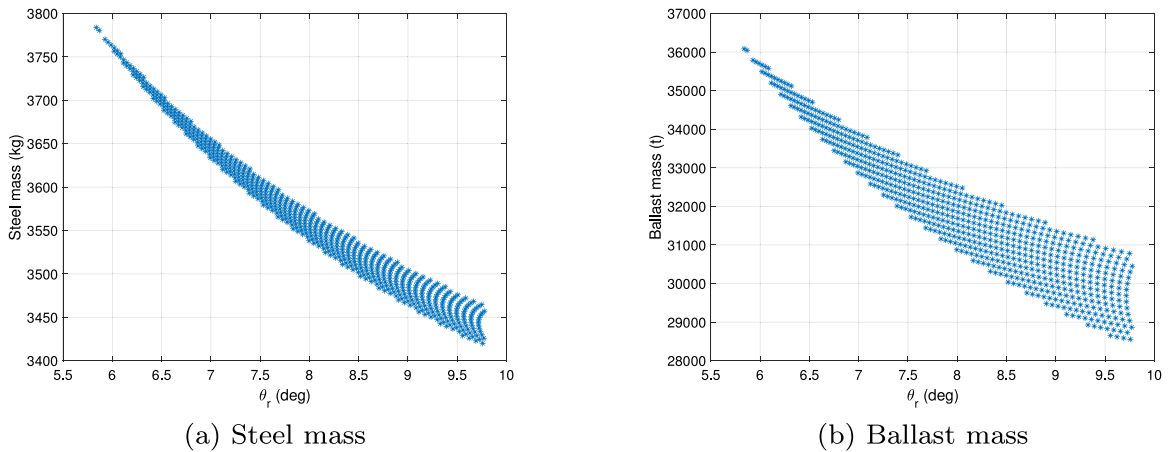


Fig. 7. Steel and ballast mass as a function of static pitch at rated wind speed, for the feasible solutions.

correspond to rotor dynamics with natural period<sup>3</sup> of 59.0 s. The natural frequencies and damping corresponding to the eigenvalues mainly associated with the nacelle motion are shown in Table 11. While for the detuned controller the amount of damping is marginal, the motion compensation approach based on Eq. (7) introduces a relative damping of 25.2% into the system. The natural frequencies, on the other hand, are very similar.

Fig. 9 compares the controllers’ performance with a time-window of the pitch motions and generator power, also for Spar6 and under turbulent wind with a mean speed of 13.0 m/s, and the associated wave conditions from Table 5. Although the instability due to controller-motion interactions is avoided by controller detuning, large resonant oscillations still are observed, due to the low level of aerodynamic damping. Large variations are also observed in the generated power. When motion compensation is used, the resonant pitch oscillations are damped out, and the variations in power are significantly reduced.

The power spectral density (PSD) of the tower base fore-aft bending moment, for the same case, is shown in Fig. 10. The pitch motions for the detuned case translate into more energy near the pitch natural frequency, as expected. The energy at the wave frequency range is similar in both cases, indicating good performance of the low-pass filter on the nacelle velocity in preventing feeding of wave-frequency components to the controller.

<sup>3</sup> With the detuned controller, the highest natural frequencies ensuring stability for Spar8 and Spar10 are 0.09 rad/s (68.0 s) and 0.08 rad/s (76.0 s), respectively.

**Table 8**

Main dimensions of the three spar FWT designs. Radii of gyration provided with respect to the origin of the body-fixed coordinate system.

	Spar6	Spar8	Spar10
Static pitch (deg)	6.0	8.0	10.0
Draft (m)	90.00	90.00	90.00
Diameter - top (m)	15.90	15.20	14.70
Diameter - bottom (m)	25.50	24.10	23.30
SWL to taper top (m)	6.00	6.00	6.00
SWL to taper bottom (m)	14.31	13.71	13.45
Ballast column height (m)	17.29	17.00	16.79
Ballast mass (kg)	$3.53 \times 10^7$	$3.10 \times 10^7$	$2.86 \times 10^7$
Steel mass (kg)	$3.77 \times 10^6$	$3.55 \times 10^6$	$3.43 \times 10^6$
GM (m)	11.89	9.82	8.40
KG (m)	30.09	32.30	33.75
KB (m)	41.91	42.05	42.09
Displacement ( $m^3$ )	$4.26 \times 10^4$	$3.82 \times 10^4$	$3.58 \times 10^4$
$C_{11}$ (N/m)	$2.39 \times 10^5$	$2.14 \times 10^5$	$2.00 \times 10^5$
$C_{33}$ (N/m)	$1.99 \times 10^6$	$1.82 \times 10^6$	$1.70 \times 10^6$
$C_{55}$ (N m/rad)	$5.09 \times 10^9$	$3.77 \times 10^9$	$3.02 \times 10^9$
$C_{66}$ (N m/rad)	$8.21 \times 10^8$	$7.13 \times 10^8$	$6.59 \times 10^8$
Mooring system mass (kg)	$6.27 \times 10^5$	$6.10 \times 10^5$	$6.01 \times 10^5$
$r_{yy}$ (m)	82.46	82.80	83.04
$r_{zz}$ (m)	11.04	10.87	10.80
$T_{surge}$ (s)	124.4	121.0	119.0
$T_{heave}$ (s)	30.8	30.3	30.3
$T_{pitch}$ (s)	38.7	44.2	49.1
1 <sup>st</sup> tower FA freq. (Hz)	0.41	0.42	0.42
2 <sup>nd</sup> tower FA freq. (Hz)	1.55	1.54	1.53

**Table 9**

Distance of platform sections from the keel, for the different spars.

Section	Distance from keel (m)		
	Spar6	Spar8	Spar10
1	13.22	13.00	12.84
2	26.15	25.15	25.75
3	34.88	32.30	33.75
4	47.98	47.27	47.69
5	57.83	56.33	57.63
6	66.77	66.42	66.72
7	79.84	80.14	80.27
8	90.00	90.00	90.00

**Table 10**

Tower section positions and sectional dimensions.

Section	Diameter (m)	Thickness (mm)	Dist. from tower base (m)	Dist. from keel (m)
1	11.74	73.4	0.00	100.00
2	11.27	70.4	17.13	117.13
3	10.55	65.9	40.38	140.38
4	9.99	62.4	55.88	155.88
5	9.15	57.6	79.13	179.13
6	8.46	52.9	102.38	202.38
7	7.87	41.0	125.63	225.63
8	7.52	47.0	141.13	241.13

**Table 11**

Natural frequency and damping for the eigenvalues mainly associated with the nacelle motion, with both controllers.

	Detuned	Motion comp.
$\omega_n$ (rad/s)	0.1519	0.1487
$\zeta$ (-)	0.0153	0.2524

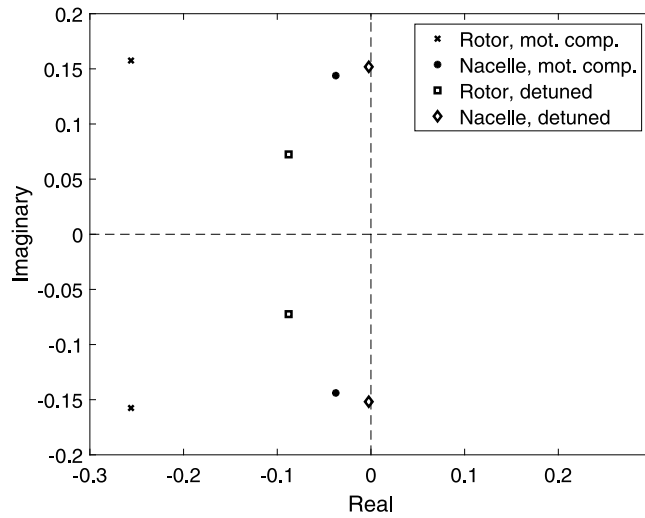
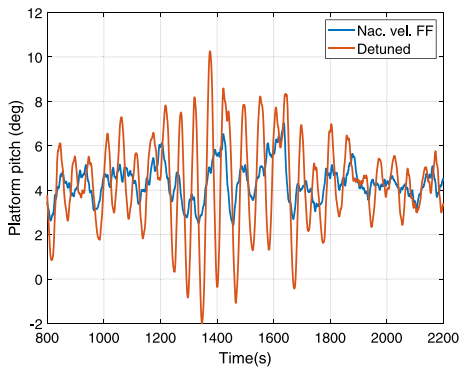
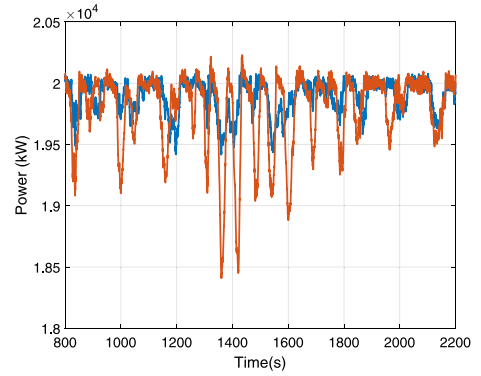


Fig. 8. Poles mainly associated with nacelle motion and rotor dynamics for the controller with motion compensation and the controller with detuned gains.  $U = 13.0$  m/s.



(a) Platform pitch



(b) Generator power

Fig. 9. Platform pitch and generator power for Spar6, using a controller with nacelle velocity feedforward and a detuned controller.  $U = 13.0$  m/s,  $H_s = 2.51$  m,  $T_p = 10.1$  s.

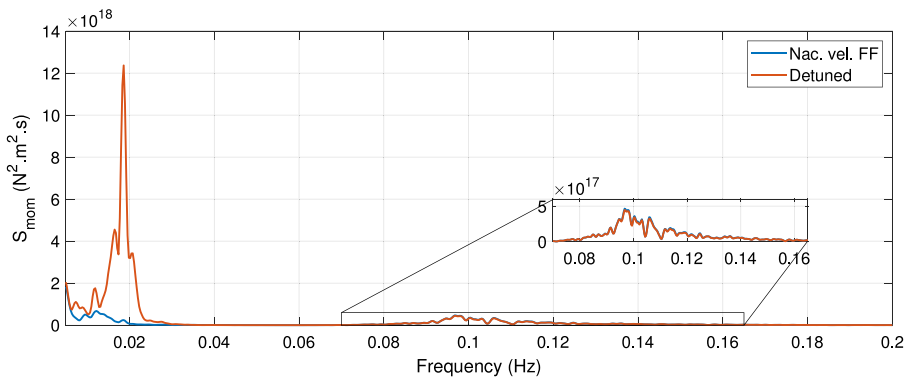


Fig. 10. Tower base fore-aft bending moment PSD for Spar6, using a controller with nacelle velocity feedforward and a detuned controller.  $U = 13.0$  m/s,  $H_s = 2.51$  m,  $T_p = 10.1$  s.

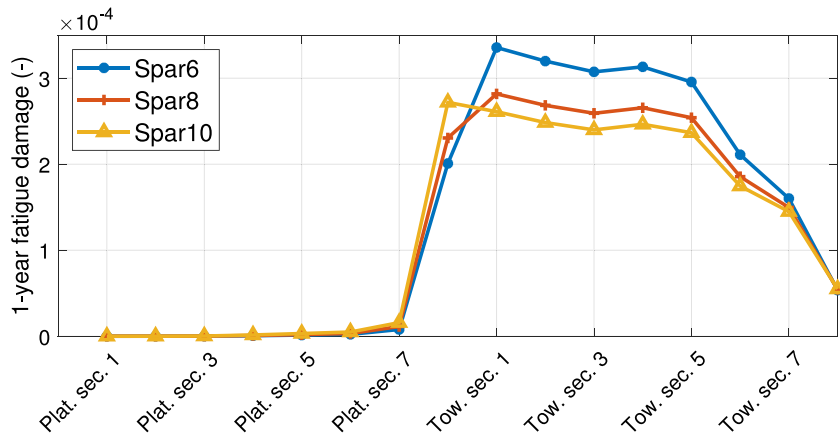
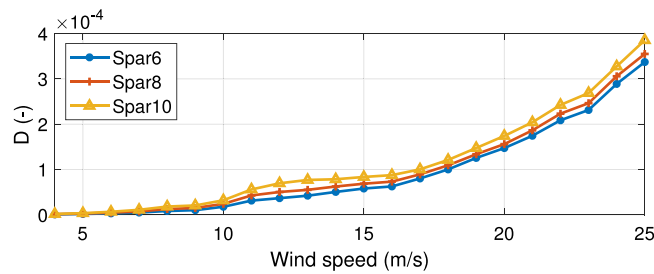
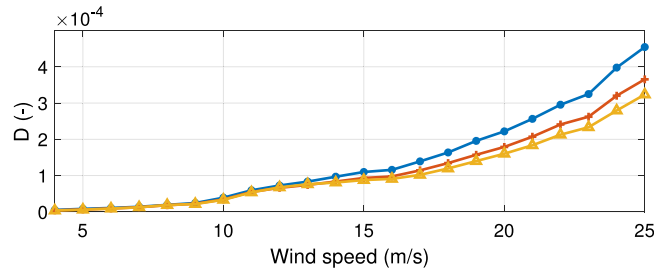


Fig. 11. Weighted sectional fatigue damage along the length of the spars.



(a) Platform section 8



(b) Tower base

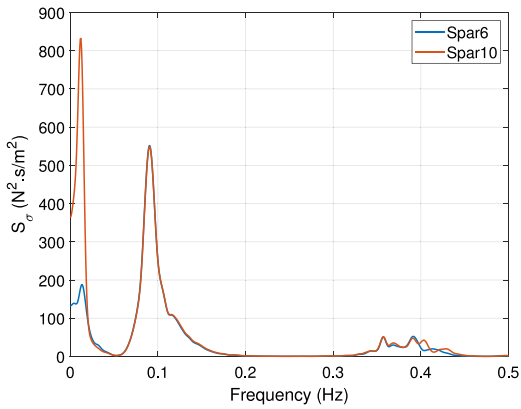
Fig. 12. One-hour fatigue damage at platform section 8 and tower base, for each of the load cases in Table 5.

6.3. Fatigue analysis

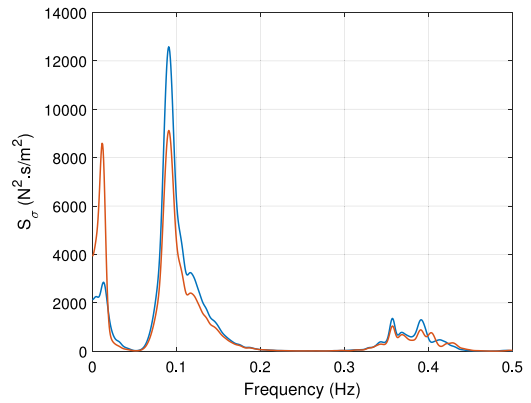
Fig. 11 shows the fatigue damage, weighted with the probabilities of occurrence in Table 5, at sections along the platform and tower. The damage for the platform sections closer to the bottom is several orders of magnitude lower than for locations near SWL. At the platform section 8, which coincides with SWL, the damage is larger for the designs with larger pitch at rated thrust (i.e., lower restoring in pitch). For the tower sections, however, the damage becomes larger for the designs with larger restoring in pitch.

The short-term damage associated with each load case is shown in Fig. 12. For the tower base, the discrepancy between the different designs is more relevant for higher wind speeds, which are associated with more severe waves. Fig. 13 shows the spectra of the axial stresses for one realization of the condition associated with  $U = 20.0$  m/s, for Spar6 and Spar10. For platform section 8, the difference between both designs is more visible for low-frequency loads, but for the tower base, the WF response is significantly larger for Spar6. A possible explanation is that Spar6 has larger WF-related RNA accelerations, due to the larger restoring in pitch. Other sections at the platform and tower show similar trends, but with lower amplitudes.

The same load cases were also analyzed without including the QTFs, thus neglecting second-order wave loads. The difference in the weighted sectional fatigue damage shown in Fig. 11 was within 0.8% for the platform sections and 0.3% for the tower sections.



(a) Platform section 8



(b) Tower base

Fig. 13. Axial stress PSD for platform section 8 and tower base -  $U = 20.0$  m/s,  $H_s = 3.4$  m,  $T_p = 8.7$  s.

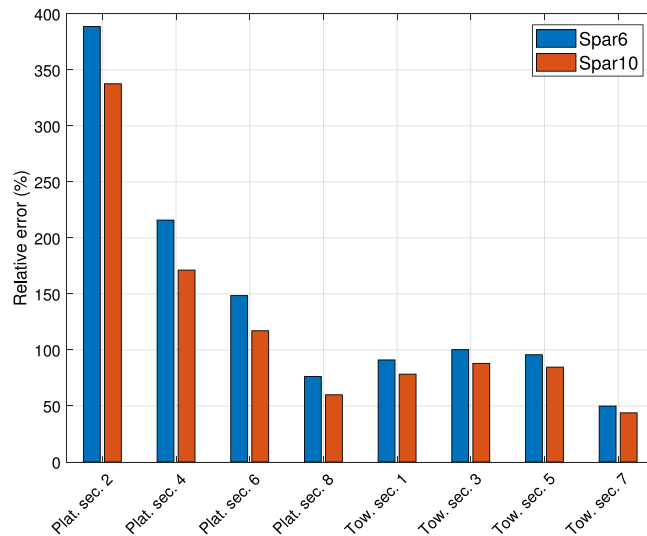


Fig. 14. Relative error in the fatigue damage obtained with the Morison formulation, compared with distributed potential theory, for Spar6 and Spar10.

6.3.1. Alternative hydrodynamic modeling with Morison formulation

Spar6 and Spar10 are also modeled with a pure Morison formulation [33], for comparison against distributed potential theory in the fatigue analysis. The same drag coefficient is used for the viscous term, while an added mass coefficient  $C_a = 1.0$  is adopted for the inertial term. Compared to potential theory, this approach neglects near-field diffraction, resulting in overestimated loads for shorter wave lengths.

Fig. 14 shows the relative error in the weighted fatigue damage, when Morison formulation is adopted, compared with distributed potential theory. Morison formulation clearly overestimates the damage for both designs, for both the platform and tower. In Fig. 15 the power spectral density of the bending moment, at the platform section 8, is shown for Spar6 modeled with both methods. The load case corresponds to mean wind speed of 20.0 m/s, with  $H_s = 3.89$  m and  $T_p = 11.1$  s. Near the peak wave frequency the moment is just slightly overestimated by Morison formulation, while the excitation from the shortest waves is amplified close to the tower 1st fore-aft bending frequency, leading to the overestimation of the fatigue damage.

6.4. Extreme analysis

The different constraints in the static pitch angle under rated thrust have significant impact on the extreme dynamics, and thus sectional stresses. Fig. 16 shows the extreme platform pitch angle and nacelle acceleration, for the three spars. The extreme pitch for Spar6 is 3.0° above the static value, while for Spar10 the increase is 4.0°—resulting in a total of 14°. The extreme nacelle acceleration for Spar6, on the other hand, is only 18% larger than for Spar10.

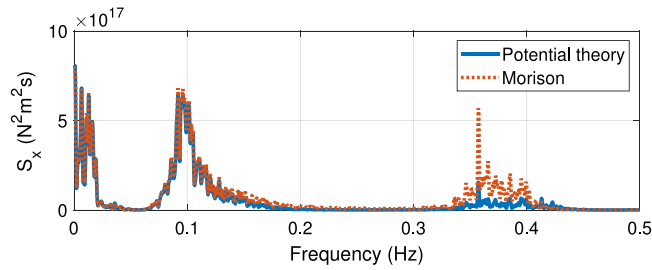
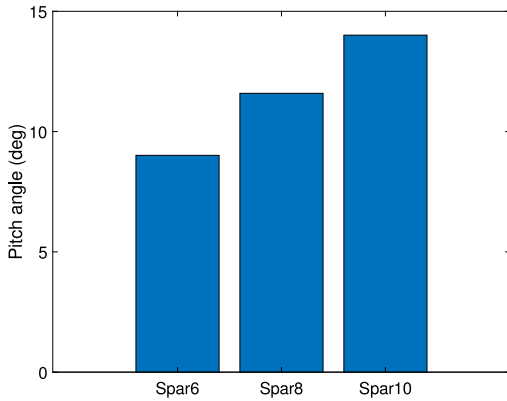
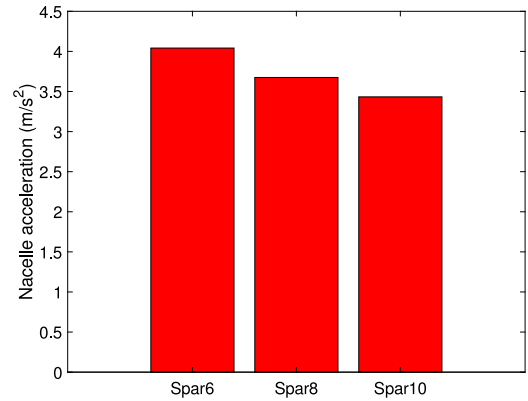


Fig. 15. Power density spectrum of bending moment at platform section 8, for Spar6, modeled with distributed potential theory and full Morison formulation.  $U = 20.0$  m/s  $H_s = 3.89$  m,  $T_p = 11.1$  s.



(a) Pitch angle



(b) Nacelle acceleration

Fig. 16. Extreme platform pitch angle and nacelle acceleration.

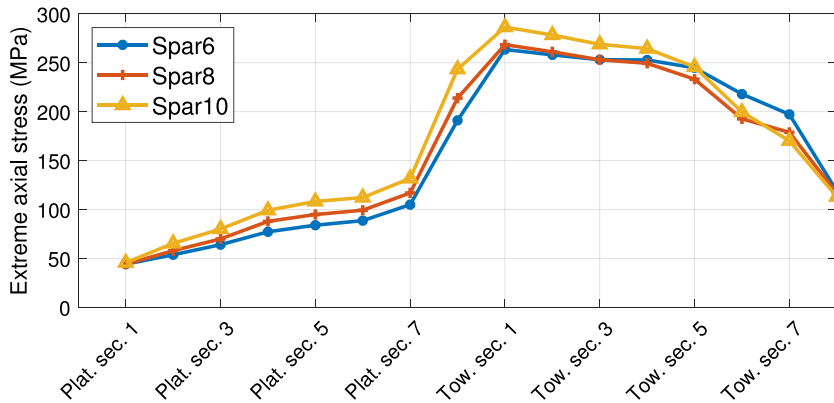


Fig. 17. Overall extreme sectional load along the length of the spars.

The extreme axial stresses along the platform and tower of all spars are shown in Fig. 17. The designs with largest static pitch angle are in general the ones with the largest extremes — except closer to the tower top, where Spar6 has the highest value. The largest differences between Spar6 and Spar10 are at the platform section 8 and at the tower base. When second-order wave loads were neglected, the difference in the extreme stresses was less than 1.3% for the platform, and less than 4.0% for the tower.

The load cases associated with the extreme stresses are shown in Table 12. For both the platform and tower, the extremes for all designs correspond to either the rated or the 50-year wind speeds — but never to conditions at the cut-off contour. For Spar6, the condition associated with 50-year wind governs the extremes at some platform sections, while for Spar8 and Spar10 all the platform extremes are associated with the rated wind speed. For the tower base, load cases at the 50-year contour govern the extremes for all designs, but for other sections along the tower the conditions associated with rated wind can be associated with the extreme loads.

**Table 12**  
Load cases associated with extreme sectional stresses for each platform (ID as defined in Table 7).

		Spar6	Spar8	Spar10
Platform	Sec. 1	i-50	v-rt	v-rt
	Sec. 2	v-rt	v-rt	v-rt
	Sec. 3	v-rt	v-rt	v-rt
	Sec. 4	v-rt	v-rt	v-rt
	Sec. 5	i-50	v-rt	v-rt
	Sec. 6	i-50	v-rt	v-rt
	Sec. 7	i-50	iv-rt	iv-rt
	Sec. 8	i-50	iv-rt	iv-rt
Tower	Sec. 1	i-50	i-50	i-50
	Sec. 2	v-rt	i-50	i-50
	Sec. 3	v-rt	i-50	i-50
	Sec. 4	v-rt	i-50	i-50
	Sec. 5	i-50	i-50	i-50
	Sec. 6	i-50	i-50	i-50
	Sec. 7	i-50	i-50	i-50
	Sec. 8	i-50	iv-rt	iv-rt

The relative importance of each contour for the different designs is also illustrated in Fig. 18, which shows the extreme axial stresses obtained with rated, cut-off, and 50-year wind speed, and associated sea states. For the platform sections, the different designs affect extreme loads at rated more significantly, due to the mean stress associated with the pitch angle at rated. For the tower, the extreme loads associated with the 50-year contour are also significantly affected by the design.

For a better understanding of the dynamic effects leading to extreme events, the axial stress time-series can be approximated as follows:

$$\sigma_{tot} \approx \sigma_{ine} + \sigma_g + \sigma_{th}, \quad (22)$$

where  $\sigma_{ine}$  is the inertial component;  $\sigma_g$  is the gravitational component; and  $\sigma_{th}$  is the component associated with the thrust.  $\sigma_{ine}$  is obtained from the acceleration time-series multiplied by the structural mass above the sections considered, while for  $\sigma_g$  the time-varying compression force and bending moments due to the structural weight are used. The thrust multiplied by the distance to the section is considered for obtaining  $\sigma_{th}$ .

Fig. 19 shows the axial stress reconstructed according to Eq. (22), for Spar6 and Spar10. Good agreement is obtained with the actual stresses, which are indicated by the dotted lines in the top subfigures. The time window shown for the platform section 8 (Fig. 19a) is extracted from a rated condition, and it is seen that the main difference is on the LF-varying gravitational component — indicating that wind loads govern the extremes at this section. For the tower base (Fig. 19b), the time window relates to a condition associated with 50-year wind. In this case, the largest differences are also observed for the gravitational component, but due to variations at the wave frequency.

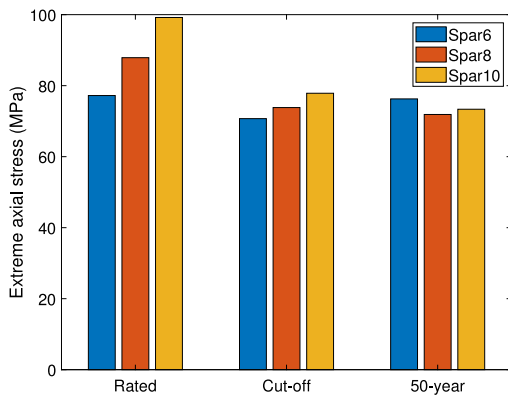
## 7. Conclusion

In this paper, three 20 MW spar FWTs are designed and compared in terms of global dynamics and structural loading along the platform and tower. The designs differ regarding the static platform pitch angle at rated wind speed,  $\theta_r$ . The entire structure is modeled as elastic, and hydrodynamic loads are distributed over the platform with a combination of potential theory and quadratic drag terms. A control system with a motion compensation strategy is adopted, avoiding the use of detuned controllers. Structural performance is assessed in terms of fatigue damage and extreme axial stresses at sections over the platform and tower length.

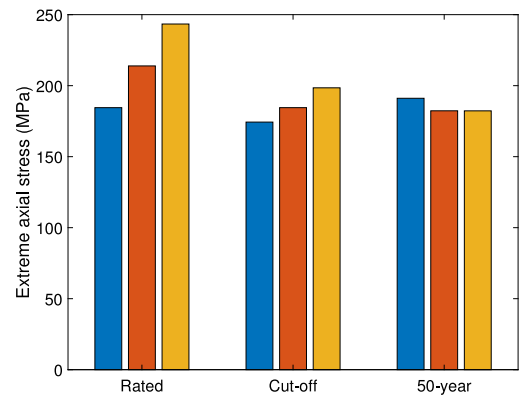
The constraint in  $\theta_r$  results in designs with distinct platform dynamics. This affects the relative contribution of inertial- and gravity-related structural loads due to the platform responses to wind and wave loads, resulting in different performance with respect to fatigue damage and extreme loads. The pitch natural periods, in general, are significantly longer than for published spar FWTs with 5 MW [46] and 10 MW [21] turbines — reaching 49.1 s for the design with  $\theta_r = 10^\circ$ .

One of the consequences of the long natural period in pitch is the inadequacy of a detuned control system, which would require an excessively low controller bandwidth, leading to unrealistic motions, structural loads, and power quality. In addition, for large FWTs the relative importance of low-frequency motions to those associated with waves increases — which also favors the use of a controller with LF motion compensation. The adoption of a motion compensation strategy, based on modifying the reference rotor speed according to the nacelle velocity, proved to be a simple and effective solution for keeping a realistic controller bandwidth, while still providing aerodynamic damping to the pitch motions. Future research within structural analysis of large FWTs should avoid the use of detuned controllers. In addition, the adoption of peak shaving also showed to be beneficial, since the extreme loads are in general associated with rated wind speed.

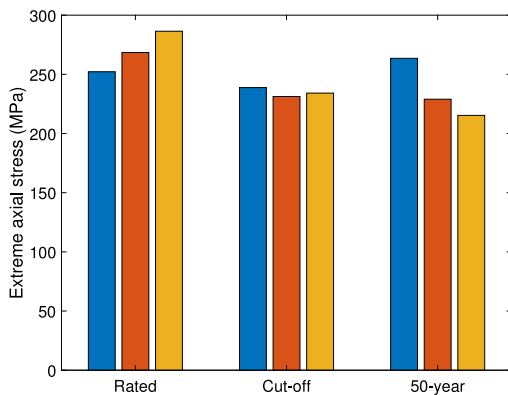
Fatigue damage was largest for platform sections closer to SWL, and also to the tower base – a similar pattern to what was previously obtained for an optimized 10 MW spar [21]. For the platform, the largest damage was observed for designs with larger  $\theta_r$ ; for the tower, larger restoring in pitch (i.e., lower  $\theta_r$ ) resulted in increased fatigue damage, and the discrepancy in damage for



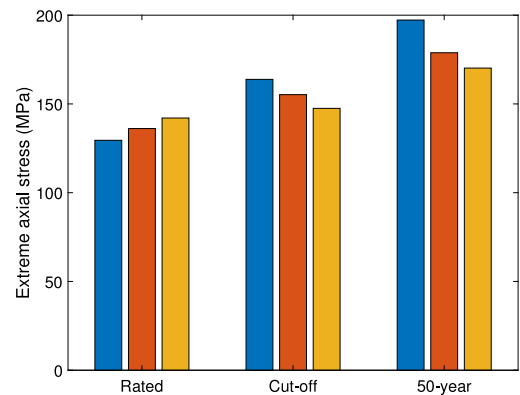
(a) Platform section 4



(b) Platform section 8



(c) Tower section 1 (base)



(d) Tower section 7

Fig. 18. Extreme axial stresses at selected platform and tower sections.

the different designs increased with the wind speed. Spectral analysis of the axial stress at the tower base, for a load case near cut-off, showed increased response at wave-frequency range for Spar6 than for Spar10, suggesting larger influence of inertial loads associated with the tower top mass.

The comparison between distributed potential theory with Morison formulation confirms the results from Engebretsen et al. [18], in that Morison formulation over-predicts the fatigue damage significantly. The overestimation is higher for the design with larger restoring in pitch. The discrepancy is related to diffraction effects, and seems to be strongly associated with excitation of the 1st tower bending frequency by short-length waves. For a cylindrical structure like a spar, the MacCamy–Fuchs formulation is expected to provide similar results as those obtained with potential theory.

For the analyses of extreme responses and axial stresses, the modified environmental contour method (MECM) proposed by Li et al. [23] was adopted, including 50-year contours associated with rated and cut-off wind speeds, as well as the 50-year wind condition. An extreme dynamic pitch angle of  $7^\circ$  was obtained for Spar6, while for Spar10 it reached  $14^\circ$ . Nacelle acceleration, on the other hand, was 18% higher for Spar6 than for Spar10.

Regarding the axial stress, the largest extreme values were observed at the platform sections at SWL and at tower base, and for the designs with largest  $\theta_r$ . The extreme axial stresses resulted from contours associated with both rated and 50-year wind speed, depending on the platform design and location of the platform/tower section. An analysis separating the relative contribution of inertial-, gravity-, and thrust-related loads showed that the difference in extreme loads between the different designs was mainly caused by the moments associated with RNA weight.

Difference-frequency second-order wave loads had limited effects on fatigue damage (0.3% for the platform and 0.8% for the tower), and small effects on the extreme stresses, (within 1.3% for the platform and 4.0% for the tower).

Previous research for 5 MW wind turbines [22,23] discarded the relevance of conditions at rated wind for extreme load analysis. The presented results confirm the need to include them in the extreme analysis of larger FWTs. The analysis also suggests that the static pitch angle under rated wind speed has large influence on fatigue damage and extreme motions and stresses. A similar study at the initial design phase of FWTs can be helpful in limiting the range of this variable, and thus reducing the design space.

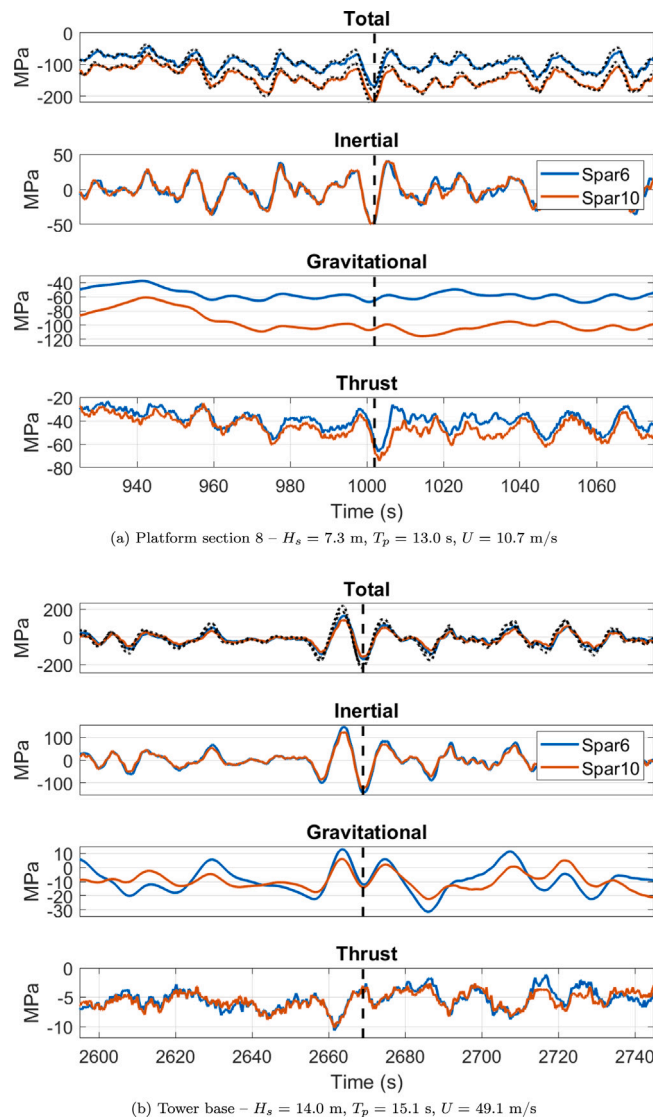


Fig. 19. Axial stress components at spar section 8 (rated) and tower base (50-year condition), reconstructed according to Eq. (22). The dotted lines on the top plots represent the original stress time series, and the vertical dashed lines indicate the instant corresponding to the extreme stress.

### Declaration of competing interest

One or more of the authors of this paper have disclosed potential or pertinent conflicts of interest, which may include receipt of payment, either direct or indirect, institutional support, or association with an entity in the biomedical field which may be perceived to have potential conflict of interest with this work. For full disclosure statements refer to <https://doi.org/10.1016/j.marstruc.2022.103182>. The first author, Carlos Eduardo Silva de Souza, is currently employed at the research institute that develops and maintains the software used for time-domain simulations (SIMA) in the paper.

### Acknowledgments

The authors are sincerely grateful to the financial support from the Department of Marine Technology of the Norwegian University of Science and Technology, the Centre for Autonomous Marine Operations and Systems, Norway (Norwegian Research Council project 223254), and SFI BLUES, Norway (NFR project 309281).

### References

- [1] State of Maine. FAQs: Gulf of Maine floating offshore wind research array. 2020, [Online; accessed 17-September-2021].

- [2] Equinor. Hywind Tampen: the world's first renewable power for offshore oil and gas. 2021, Online; accessed 2021-09-05.
- [3] Principle Power. Projects - Principle Power, Inc.. 2021, [Online; accessed 17-September-2021].
- [4] General Electric. Haliade-X offshore wind turbine - The world's most powerful offshore turbine built today. 2021, Online; accessed 2021-09-05.
- [5] MingYang Smart Electric. Leading innovation: MingYang Smart Energy launches MySE 16.0-242, the world's largest offshore Hybrid Drive wind turbine. 2021, Online; accessed 2021-09-05.
- [6] Ashuri T, Martins JRRA, Zaaier MB, van Kuik GAM, van Bussel GJW. Aeroservoelastic design definition of a 20 MW common research wind turbine model. *Wind Energy* 2016;19(11):2071–87, we.1970.
- [7] Jensen PH, Chaviaropoulos T, Natarajan A, Rasmussen F, Madsen HA, Jamieson P, Wingerden JW, Riziotis V, Barlas A, Polinder H, Abrahamsen AB, Powell D, Zinderen GJ, Kaufer D, Shirzadeh R, Armendariz JA, Voutsinas S, Manjock A, Paulsen US, Dobbin J, Potestio S. LCOE reduction for the next generation offshore wind turbines - outcomes from the INNWIND.EU project. tech. rep., INNWIND.EU; 2017.
- [8] Sartori L, Bellini F, Croce A, Bottasso C. Preliminary design and optimization of a 20MW reference wind turbine. *J Phys Conf Ser* 2018;1037:042003.
- [9] Qin CC, Loth E, Zalkind DS, Pao LY, Yao S, Griffith DT, Selig MS, Damiani R. Downwind coning concept rotor for a 25 MW offshore wind turbine. *Renew Energy* 2020;156:314–27.
- [10] Yao S, Chetan M, Griffith DT, Mendoza ASE, Selig MS, Martin D, Kianbakht S, Johnson K, Loth E. Aero-structural design and optimization of 50 MW wind turbine with over 250 m blades. *Wind Eng* 2021;July 2021:1–23.
- [11] Jonkman J, Butterfield S, Musial W, Scott G. Definition of a 5-MW reference wind turbine for offshore system development. Tech. Rep. NREL/TP-500-38060, Colorado, United States: National Renewable Energy Laboratory; 2009.
- [12] Bak C, Zahle F, Bitsche R, Kim T, Yde A, Henriksen LC, Natarajan A, Hansen MH. Description of the DTU 10 MW reference wind turbine. Tech. Rep. DTU Wind Energy Report-I-0092, DTU Wind Energy; 2013.
- [13] Veers P, Dykes K, Lantz E, Barth S, Bottasso CL, Carlson O, Clifton A, Green J, Green P, Holtinen H, Laird D, Lehtomäki V, Lundquist JK, Manwell J, Marquis M, Meneveau C, Moriarty P, Munduate X, Muskulus M, Naughton J, Pao L, Paquette J, Peinke J, Robertson A, Rodrigo JS, Sempreviva AM, Smith JC, Tuohy A, Wisler R. Grand challenges in the science of wind energy. *Science* 2019;366(6464). eaau2027.
- [14] Svendsen K. Structural design and dynamic analysis of a tension leg platform wind turbine, considering elasticity in the hull (Master's thesis), Norwegian University of Science and Technology / TU Delft; 2016.
- [15] Borg M, Hansen AM, Bredmose H. Floating substructure flexibility of large-volume 10MW offshore wind turbine platforms in dynamic calculations. *J Phys Conf Ser* 2016;753(8).
- [16] Luan C, Gao Z, Moan T. Development and verification of a time-domain approach for determining forces and moments in structural components of floaters with an application to floating wind turbines. *Mar Struct* 2017;51:87–109.
- [17] Hegseth JM, Bachynski EE, Karimirad M. Comparison and validation of hydrodynamic load models for a semi-submersible floating wind turbine. In: Proceedings of the ASME 2018 37th international conference on ocean, offshore and arctic engineering. 2018.
- [18] Engebretsen E, Haslum H, Aagaard O. Distributed potential theory and its application for spar-type floating offshore wind turbines. In: Proceedings of the ASME 2020 39th international conference on ocean, offshore and arctic engineering (Virtual conference), 2020.
- [19] Kvittem MI. Modelling and response analysis for fatigue design of a semi-submersible wind turbine (Ph.D. thesis), Trondheim, Norway: Norwegian University of Science and Technology; 2014.
- [20] Kvittem MI, Moan T. Time domain analysis procedures for fatigue assessment of a semi-submersible wind turbine. *Mar Struct* 2015;40(Supplement C):38–59.
- [21] Hegseth JM, Bachynski EE, Martins JR. Integrated design optimization of spar floating wind turbines. *Mar Struct* 2020;72:102771.
- [22] Karimirad M, Moan T. Extreme dynamic structural response analysis of catenary moored spar wind turbine in harsh environmental conditions. *J Offshore Mech Arct Eng* 2011;133(4):041103.
- [23] Li Q, Gao Z, Moan T. Modified environmental contour method to determine the long-term extreme responses of a semi-submersible wind turbine. *Ocean Eng* 2017;142:563–76.
- [24] Nielsen F, Hanson T, Skaare B. Integrated dynamic analysis of floating offshore wind turbines. In: Proceedings of the ASME 2016 25th international conference on offshore mechanics and arctic engineering. 2006.
- [25] Larsen TJ, Hanson TD. A method to avoid negative damped low frequent tower vibrations for a floating, pitch controlled wind turbine. *J Phys Conf Ser* 2007;75:012073.
- [26] Jonkman JM. Influence of control on the pitch damping of a floating wind turbine. In: Proceedings of the ASME wind energy symposium. 2008.
- [27] Skaare B, Hanson TD, Nielsen FG. Importance of control strategies on fatigue life of floating wind turbines. In: Proceedings of the ASME 2007 26th international conference on ocean, offshore and arctic engineering. 2007, p. 493–500.
- [28] Lackner MA. An investigation of variable power collective pitch control for load mitigation of floating offshore wind turbines. *Wind Energy* 2013;16(4):519–28.
- [29] Hegseth JM, Bachynski EE, Martins JRRA. Design optimization of spar floating wind turbines considering different control strategies. *J Phys Conf Ser* 2020;1669:012010.
- [30] Hsu C-G. Substructure models for dynamic analysis of floating wind turbines and the effect of hull flexibility (Master's thesis), Norwegian University of Science and Technology / TU Delft; 2019.
- [31] DNV-GL. Design of floating wind turbine structures (DNVGL-ST-0119). DNV-GL AS; 2018.
- [32] LKAB Minerals AB. High density concrete. 2019.
- [33] Faltinsen O. Sea loads on ships and offshore structures. Cambridge ocean technology series, Cambridge University Press; 1993.
- [34] Newman J. Marine hydrodynamics. The Massachusetts Institute of Technology; 1977.
- [35] NREL. Rosco. Version 1.0.0. 2020.
- [36] Skaare B, Nielsen FG, Hanson TD, Yttervik R, Havmøller O, Rekdal A. Analysis of measurements and simulations from the Hywind Demo floating wind turbine. *Wind Energy* 2015;18(6):1105–22.
- [37] Lenfest E, Goupee A, Wright A, Abbas N. Tuning of nacelle feedback gains for floating wind turbine controllers using a two-dof model. In: Proceedings of the ASME 2020 39th international conference on ocean, offshore and arctic engineering. 2020.
- [38] Fischer B, Shan M. A survey on control methods for the mitigation of tower loads. Tech. Rep. Project report 01/104256, Kassel, Germany: Fraunhofer-institute for wind energy and energy systems technology, IWES; 2013.
- [39] Borg M, Bredmose H, Hansen AM. Elastic deformations of floaters for offshore wind turbines: dynamic modelling and sectional load calculations. In: Proceedings of the ASME 2017 36th international conference on ocean, offshore and arctic engineering. 2017.
- [40] Hegseth JM, Bachynski EE. A semi-analytical frequency domain model for efficient design evaluation of spar floating wind turbines. *Mar Struct* 2019;64:186–210.
- [41] Ormberg H, Larsen K. Coupled analysis of floater motion and mooring dynamics for a turret-moored ship. *Appl Ocean Res* 1998;20(1):55–67.
- [42] SINTEF OCEAN. RIFLEX - Theory manual. 2016.
- [43] Hansen M. Aerodynamics of wind turbines. Earthscan; 2013.
- [44] SINTEF OCEAN. SIMO - Theory manual. 2016.
- [45] Cook R. Concepts and applications of finite element analysis. 4th ed.. Wiley; 2001.
- [46] Jonkman J. Definition of the floating system for phase IV of OC3. Tech. Rep. NREL/TP-500-47535, Colorado, United States: National Renewable Energy Laboratory; 2010.

- [47] WAMIT. WAMIT user manual. Chestnut Hill, United States; 2006.
- [48] Cummins WE. The impulse response and ship motions. In: Symposium on ship theory. 1962.
- [49] Ogilvie TF. Recent progress toward the understanding and prediction of ship motions. tech. rep., Washington D.C., USA: David W. Taylor Model Basin; 1964.
- [50] Taghipour R, Perez T, Moan T. Hybrid frequency–time domain models for dynamic response analysis of marine structures. *Ocean Eng* 2008;35(7):685–705.
- [51] DNV. Environmental conditions and environmental loads (DNV-RP-C205). Det Norske Veritas; 2010.
- [52] Simos AN, Ruggeri F, Watai RA, Souto-Iglesias A, Lopez-Pavon C. Slow-drift of a floating wind turbine: An assessment of frequency-domain methods based on model tests. *Renew Energy* 2018;116(Part A):133–54.
- [53] Newman J. Second-order, slowly-varying forces on vessels in irregular waves. Tech. Rep. MIT Paper 19, Cambridge, United States: Massachusetts Institute of Technology; 1974.
- [54] Li L, Gao Z, Moan T. Joint environmental data at five European offshore sites for design of combined wind and wave energy devices. In: Proceedings of the ASME 2013 32nd international conference on ocean, offshore and arctic engineering. 2013.
- [55] Jonkman BJ, Kilcher L. TurbSim user's guide: version 1.06.00. tech. rep., National Renewable Energy Laboratory; 2012.
- [56] IEC. Wind energy generation systems – Part 3-2 Design requirements for floating offshore wind turbines. International Electrotechnical Commission; 2019.
- [57] DNV. Fatigue design of offshore steel structures (DNV-RP-C203). Det Norske Veritas; 2011.
- [58] WAFO-group. WAFO - A matlab toolbox for analysis of random waves and loads - A tutorial for version 2017. Lund, Sweden: Math. Stat., Center for Math. Sci., Lund Univ.; 2017.